# Adenine and D-Ribose Coderived Activated Carbon with N-Methyl-2-Pyrrolidone-Modified Aqueous Electrolyte for Long-Life Zinc-Ion Capacitors

Li Tao, Chun Li,* Xuejun Lu, Rameez Ahmad Mir, Nieves López-Salas, and Jian Liu

Aqueous zinc (Zn)-ion capacitors (AZICs) have addressed considerable attention due to their high energy density, low toxicity, and rich abundance of Zn metal. However, the development of ultra-long cycle life and high energy density AZICs is often hindered by the lack of adequately optimized active carbon (AC) electrodes and compatible electrolytes. Herein, high-performance, free-standing AC electrodes for AZICs are derived from sustainable precursors—adenine and D-ribose—using magnesium chloride hexahydrate as an activation agent via a eutectic template strategy. Furthermore, an aqueous hybrid electrolyte tailored to the designed AC electrodes is developed, significantly enhancing the stability and cycle life of AZICs. The resulting AZIC achieves a high specific capacity of 164.39 F g$^{-1}$ at 0.1 A g$^{-1}$ and a magnificently long cell life of over 50 000 cycles with nearly 94.5% capacitance retention at 10 000$^{th}$ cycles, and 76.3% at 50 000$^{th}$ cycle. The pouch cell assembly also demonstrates comparable specific capacitance and energy density to the coin cell, underscoring the potential of large-scale applications of AZICs.

## 1. Introduction

In today's fast-evolving world, the demand for efficient, sustainable, and safe energy storage solutions has become pivotal in numerous industries such as healthcare, automotive, and telecommunications.[1–4] Due to relatively abundant resources and high stability in the atmosphere, zinc (Zn), various aqueous Zn-ion batteries (AZIB), and aqueous Zn-ion capacitors (AZICs) systems researched with promising results potentially lead to significant advancements in the realm of energy storage. AZICs usually contain very similar configurations to AZIBs, with Zn as the anode and capacitive carbon as the cathode.[5] However, AZICs' capacitances are dominated mainly by capacitive behaviors instead of intercalation processes, typically found in AZIBs.[6–8] One of the most notable advantages of AZIC is the compatibility of water-based electrolytes.[9] The adoption of water in electrolytes not only can drastically reduce the usage of toxic organic solvents but also enhance cell performance and ease the production process.[10,11] In AZICs, capacitance storage capability and operating voltage range are highly related to the use and design of active carbon (AC) materials and electrolytes.[10,12,13] Although combining high-performance electrolytes with advanced AC materials has the potential to significantly enhance AZIC performance, progress is still limited by the lack of integrated studies and material optimization.

To address these challenges, we employed a high-porosity and a high-performance AC using a eutectic template strategy. This strategy used a mixture of adenine ($C_5H_5N_5$) and D-ribose ($C_5H_{10}O_5$) in various ratios as the carbon precursors, combined with the selected crystalline water-containing salts, $MgCl_2 \cdot 6H_2O$ and $CaCl_2 \cdot 2H_2O$, as activation salts and templates. Adenine, a nitrogen-rich molecule, introduces heteroatoms (e.g., nitrogen) into the carbon framework, enhancing surface properties such as wettability and electronic conductivity. D-ribose, as a carbohydrate, acts as a carbon source and facilitates the formation of the eutectic mixture with the crystalline water-containing salts to generate a uniform porous structure during pyrolysis. The eutectic mixture ensures homogeneous carbonization and efficient pore formation by offering a semiliquid environment prior to precursor decomposition. During carbonization, $MgCl_2$ or $CaCl_2$ serves as a hard template, generating a highly porous structure with optimized surface area and pore size distribution, key factors for enhancing the electrochemical performance of AC in AZICs.

Herein, we present a comprehensive study on the synthesis and optimization of high-performance AC materials for AZIC applications. The activation process mediated by $MgCl_2 \cdot 6H_2O$ and $CaCl_2 \cdot 2H_2O$ yields materials with excellent porosity and tailored structural properties, paired with a hybrid aqueous electrolyte[14] to achieve a highly competitive voltage window of 1.7 V and an ultra-long cycling life of 50 000 cycles in a full Zn//AC AZIC cell. Our approach demonstrates a compelling combination of innovation and practicality, offering new insights into material design for next-generation energy storage devices.

*L. Tao, X. Lu, R. A. Mir, J. Liu*
*School of Engineering, Faculty of Applied Science*
*The University of British Columbia*
*3333 University Way, Kelowna BC V1V 1V7, Canada*

*C. Li, N. López-Salas*
*Department o Chemistry, Sustainable Materials Chemistry Group*
*University of Paderborn*
*Warburguer strasse 100, 33098 Paderborn, Germany*
*E-mail: cli2527@uwo.ca*

## 2. Results and Discussion

Figure 1a–d presents transmission electron microscopy (TEM) images of the four porous carbon materials synthesized with different precursor ratios and salts, showcasing distinct structural and morphological features influenced by the synthesis process. Figure 1a,b depicts the $A_2R9Mg$ and $AR_29Mg$ samples, respectively, which exhibit prominent tube-like mesopores. These structures result from the use of $MgCl_2 \cdot 6H_2O$ as both a molten salt and a hard template. During synthesis, the precursor undergoes polymerization and carbonization within the layered structure of $MgCl_2 \cdot 6H_2O$. The presence of a semiliquid eutectic mixture, formed by the interaction of D-ribose, and crystalline water, allows for efficient diffusion of the precursors between $MgCl_2$ layers, facilitating the creation of well-aligned tubular mesopores.[15] The $AR_29Mg$ sample (Figure 1b), with a higher D-ribose ratio, enhances this effect by generating a more uniform and extensive semiliquid environment during synthesis, resulting in a more interconnected and regular tube-like mesoporous network.

In contrast, Figure 1c,d shows the $AR_29Ca$ and $A_2R9Ca$ samples, prepared with $CaCl_2 \cdot 2H_2O$ as the molten salt. Both samples exhibit uniformly distributed round mesopores with multilayered graphitic walls. The synthesis process for these samples also involves the formation of hydrogen bonds between D-ribose and the crystalline water of $CaCl_2 \cdot 2H_2O$, creating a semiliquid eutectic environment prior to the polymerization and carbonization of the precursors.[16] As carbonization progresses, $CaCl_2$ nanoparticles precipitate and act as hard templates, promoting the development of mesopores. For $AR_29Ca$ (Figure 1c), the relatively lower D-ribose content results in a less interconnected mesoporous structure, while in $A_2R9Ca$ (Figure 1d), the higher

D-ribose ratio facilitates the formation of a more extensive eutectic mixture, producing a more developed mesoporous network with graphitic layers serving as robust walls. These observations underscore the critical role of precursor ratios, salts, and the eutectic template strategy in controlling pore morphology and graphitic structure, which could directly influence the electrochemical performance of the resulting materials.

To better understand the role of salt templates in shaping the pore structure, we compared our eutectic templating strategy with traditional methods such as KOH activation and metal organic framework (MOF)-derived templating. While KOH activation typically yields high surface areas, it lacks control over pore architecture and involves harsh chemicals. MOF templates can offer tunable porosity but often require complex synthesis procedures and high cost. In contrast, our approach employs hydrated salts ($MgCl_2 \cdot 6H_2O$ or $CaCl_2 \cdot 2H_2O$) and bio-based precursors to generate a semiliquid eutectic phase at low temperatures, facilitating uniform dispersion and confined polymerization of carbon precursors. $MgCl_2 \cdot 6H_2O$ enables the formation of layered domains that guide precursor diffusion and result in tubular microporous structures, as observed in both TEM and scanning electron microscopy (SEM) images (Figure 1a,b, S1a,b, Supporting Information). Conversely, $CaCl_2 \cdot 2H_2O$ promotes the development of 2D graphitic nanosheets with mesopores (Figure 1c,d, S1c,d, Supporting Information), likely due to salt recrystallization acting as hard templates. This mechanism is in agreement with previous studies reporting directional graphitization via salt-hydrate eutectic templating.[17] These salt-dependent morphological differences are further reflected in the $N_2$ adsorption data: $MgCl_2$-derived carbons exhibit higher micropore volumes and narrower pore size distributions, while $CaCl_2$-based materials show broader mesopore distributions and higher
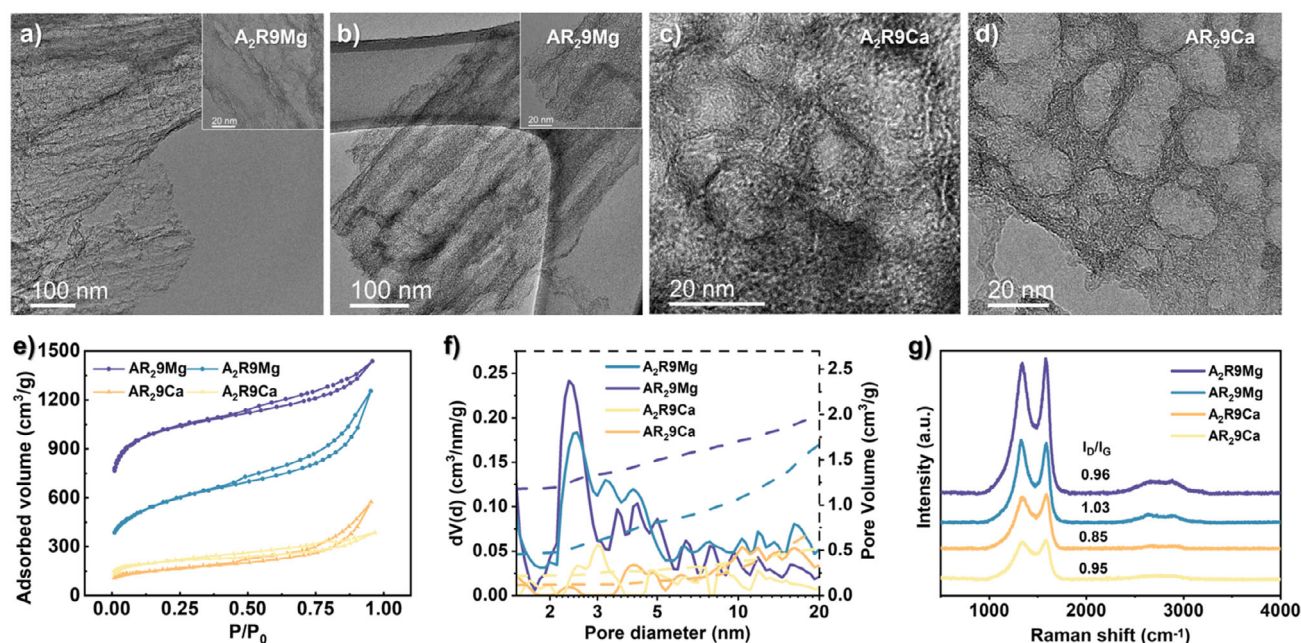


**Figure 1.** TEM images of a) $AR_29Mg$, b) $A_2R9Mg$, c) $AR_29Ca$, d) $A_2R9Ca$, and e) 77 K nitrogen adsorption–desorption isotherms, f) QSDFT pore size distributions obtained from the adsorption branch of $N_2$ adsorption isotherms, and g) Raman spectra for respective active carbon materials.

**Table 1.** BET data and $I_D/I_G$ ratio of AR$_2$9Mg, A$_2$R9Mg, AR$_2$9Ca, and A$_2$R9Ca.

| Sample | $S_{BET}$ [m² g⁻¹] | Micropore volume [cm² nm g⁻¹] | Mesopore volume [cm³ nm g⁻¹] | $V_T$ [cc g⁻¹] | $I_D/I_G$ ratio |
|---|---|---|---|---|---|
| AR$_2$9Mg | 3823.00 | 1.19 | 0.87 | 2.06 | 0.96 |
| A$_2$R9Mg | 2027.00 | 0.47 | 1.35 | 1.82 | 1.03 |
| AR$_2$9Ca | 557.00 | 0.12 | 0.72 | 0.84 | 0.85 |
| A$_2$R9Ca | 753.00 | 0.22 | 0.34 | 0.56 | 0.95 |

graphitic ordering. Together, these results confirm the dual function of the hydrated salts as both structure-directing agents and porosity modulators, offering a controllable and scalable route for tailoring carbon architectures.

The N$_2$ adsorption and desorption isotherms in Figure 1e show that all four samples showed typical type I and type IV adsorption/desorption isotherms.[18] Pore size and volume distribution are plotted in Figure 1f, with Brunauer-Emmett-Teller (BET) data listed in **Table 1**. AR$_2$9Mg and A$_2$R9Mg displayed much higher adsorption volumes than A$_2$R9Ca and AR$_2$9Ca. Both AR$_2$9Mg and A$_2$R9Mg exhibited sharp increases at the low-pressure range ($P/P_0 < 0.02$) and steady increases up to $P/P_0 = 0.45$, suggesting their higher microspore content.[18] Between AR$_2$9Mg and A$_2$R9Mg, AR$_2$9Mg showed a higher initial adsorption volume ($\approx$750 cm³) and a steeper rise at a lower pressure range, suggesting a larger total pore volume ($V_T$) and more extensive micropore formation. This observation aligns with Table 1 data and can be attributed to different salts.

Figure 1f highlights the distinct pore structures of samples synthesized with MgCl$_2$·6H$_2$O and CaCl$_2$·2H$_2$O. The hysteresis loops in the $0.45 < P/P_o < 0.95$ range are characteristic of mesopores, with MgCl$_2$-derived samples (A$_2$R9Mg and AR$_2$9Mg) exhibiting higher micropore volumes, while CaCl$_2$-derived samples (A$_2$R9Ca and AR$_2$9Ca) show much lower micropore and mesopore volumes than the formers. The sharp rise in adsorption at $0.85 < P/P_o < 0.95$ for A$_2$R9Mg and AR$_2$9Ca indicates a higher percentage of macropores compared to AR$_2$9Mg and A$_2$R9Ca, which show smoother transitions in this range.[19,20] Notably, despite AR$_2$9Ca containing a higher proportion of macropores, its $V_T$ is significantly lower than that of MgCl$_2$-derived samples, underscoring the efficiency of MgCl$_2$ in facilitating micropore formation.

Although at a glance, the AR$_2$9Mg has the largest surface area at 3823.00 m² g⁻¹, which generally is considered one of the critical factors for a high-performance electrode,[21] the pore volume, size distribution, and level of graphitization are also critical factors in ZIC systems.[22] A close study of the pore diameter plots in Figure 1f and Table 1 showed that AR$_2$9Mg has a higher distribution ($\approx$57.76%) of pore size smaller than 2 nm in diameter, which according to Table 1, at 1.19 cc g⁻¹, is the highest among all samples. A$_2$R9Mg has a relatively close $V_T$ to the AR$_2$9Mg at 1.82 cc g⁻¹; however, both the figure and the data table suggest that most of these pores ($\approx$74.17%) are larger than 2 nm, which falls into the mesopore range. When comparing the $I_D/I_G$ ratio, A$_2$R9Mg is more amorphous with a 1.03 ratio, while AR$_2$9Mg is more graphitized with a ratio of 0.96. AR$_2$9Ca and A$_2$R9Ca have a relatively low specific area

and pore volume, with AR$_2$9Ca at 557.00 m² g⁻¹, 0.84 cc g⁻¹, and A$_2$R9Ca at 753.00 m² g⁻¹, 0.56 cc g⁻¹. Between these two samples, AR$_2$9Ca has a high mesopore composition (85.7%), while A$_2$R9Ca has a lower composition at 60.7%. The $I_D/I_G$ ratio of A$_2$R9Ca at 0.95 is relatively close to A$_2$R9Mg and AR$_2$9Mg. However, with a ratio of 0.85, AR$_2$9Ca is much more graphitized than all other samples.

X-ray photoelectron spectroscopy (XPS) was performed on A$_2$R9Mg for surface elemental composition identification and its chemical states. The survey spectra in Figure S2a, Supporting Information, showed the existence of principle C 1s, O 1s, and N 1s. Three peaks are fitted in the C 1s spectrum at 286.1, 285.1, and 284.5 eV, as shown in Figure S2b, Supporting Information, representing C—N, C—O, and C—C, respectively. Two peaks at 532.7 and 531.4 eV can be fitted in the O 1s spectrum in Figure S2c, Supporting Information, representing phenol groups (C—OH) and quinone-type groups (C=O).[23] For N 1s, three peaks can be fitted at 401.1, 399.7, and 398.1 eV, representing quaternary-N (N-Q), pyrrolic-N (N-5), and pyridinic-N (N-6), respectively (Figure S2d, Supporting Information).[23,24] The content of O 1s (at 4.4%) is commonly seen in activated carbons (ACs). However, the distinct content of N 1s (at 4%) suggests a content of various N-species, a characteristic of protein-rich precursor-derived carbons that are not typically found in commercial ACs.[16]

Typical D ($\approx$1300 cm⁻¹) and G ($\approx$1600 cm⁻¹) bands are found in the Raman spectra across all samples (Figure 1f). The ratio relationship between D and G peaks provides information about carbon material structures.[25] The D band represents disordered carbons from sp³carbons, and the G band is related to ordered carbon structures.[26] Intensity ratio $I_D/I_G$ for A$_2$R9Mg, AR$_2$9Mg, A$_2$R9Ca, and AR$_2$9Ca is calculated as 0.96, 1.03, 0.85, and 0.95, respectively (Table 1), suggesting that MgCl$_2$·6H$_2$O as an activating agent creates more amorphous carbon than CaCl$_2$·2H$_2$O. The ratio between adenine and D-ribose also alters the graphite degree, with the 1:2 ratio generating a higher graphite degree for both activation salts than the 2:1 ratio.

Cyclic voltammetry (CV) was tested at 10 mV s⁻¹ with voltage windows of 0.2–1.9 V to assess each material's electrochemical behavior in Zn-ion capacitors. All samples had similar near-rectangular shapes, with a slight hump between 1.1 and 1.2 V, which might be caused by certain redox processes.[27] A$_2$R9Mg delivered the highest current range, around 1.5 A g⁻¹ during charge and 1.7 A g⁻¹ during discharge (**Figure 2**a). AR$_2$9Mg performs slightly worse than A$_2$R9Mg, with 1.25 A g⁻¹ during charge and 1.5 A g⁻¹ during discharge. A$_2$R9Ca and AR$_2$9Ca had almost identical performance; however, they are much worse than A$_2$R9Mg and AR$_2$9Mg, likely caused by much lower hierarchical porosity.[20,28,29] Electrochemical impedance spectroscopy (EIS) revealed that the A$_2$R9Mg has the lowest internal resistance (0.01 ohm); however, it has considerably higher transfer resistance (Figure 2b). While A$_2$R9Mg did not have the largest $V_T$ or BET surface area according to the data in Table 1, it exhibited the highest mesopore volume, favoring ion adsorption/desorption kinetics in AZIC systems.[22,30,31]

Once the A$_2$R9Mg was deemed the best-performed sample, electrolytes were tested to optimize energy storage capability and cycling life. 2 molality (m) zinc trifluoromethanesulfonate
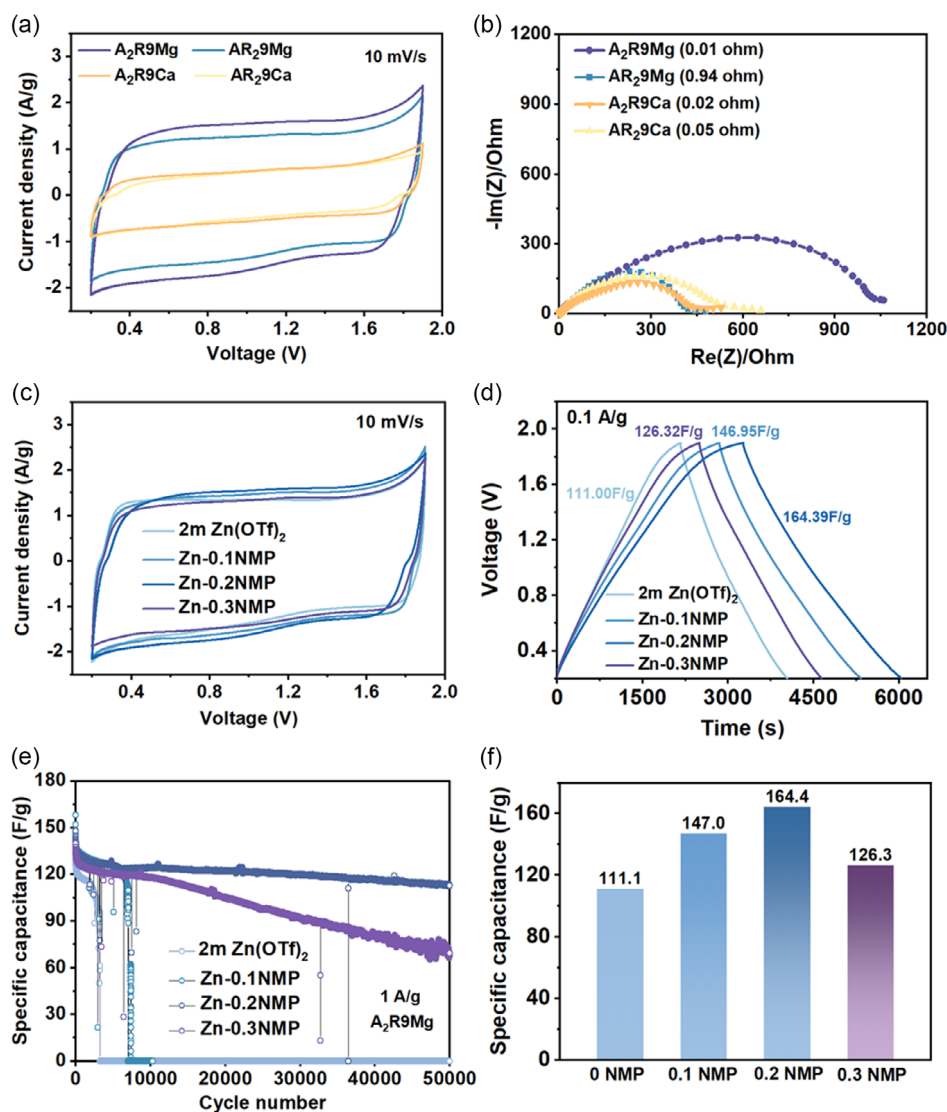
**Figure 2.** a) CV and b) EIS for $A_2R9Mg$, $AR_29Mg$, $AR_29Ca$, and $A_2R9Ca$. c) CV, d) GCD, e) long-cycling, and f) specific capacitance bar chart of $A_2R9Mg$ in 2 m $Zn(OTF)_2$, Zn-0.1NMP, Zn-0.2NMP, and Zn-0.3NMP electrolytes.

$(Zn(OTF)_2)$ in water was used as the standard electrolyte (2 m $Zn(OTF)_2$), and N-methyl-2-pyrrolidone (NMP) as an additive was added with molar ratio of NMP:$H_2O = 0.1:1$, 0.2:1, and 0.3:1, which corresponds to Zn-0.1NMP, Zn-0.2NMP, and Zn-0.3NMP, respectively. CV tests performed at 10 mV s$^{-1}$ (Figure 2c) indicated that all modified samples delivered similar performance without significantly altering the profile from the standard electrolyte and specific current, with Zn-0.2NMP taking a slight advantage. During the galvanostatic charging–discharging (GCD) test (Figure 2d), the Zn-0.2NMP outperformed other samples with superior performance. Tested under 0.1 A g$^{-1}$, all samples showed nearly no voltage drop upon discharging and a similarly linear charge/discharge profile. However, the Zn-0.2NMP electrolyte delivered the longest charge/discharge time without noticeable disfiguring the charge/discharge profile. Calculations have been performed based on GCD data to obtain each sample's specific capacity (F g$^{-1}$), which is noted in Figure 2d and visualized in Figure 2f. The sample with Zn-0.2NMP

electrolyte has a specific capacitance of 164.4 F g$^{-1}$, outperforming all other samples. A rate-performance test was also performed on samples with different electrolytes and the results are plotted in Figure S4, Supporting Information. All samples had similar trends under different current rates; however, slight performance differences can be observed. Zn-0.1NMP and Zn-0.2NMP electrolyte exhibited a near-identical performance, with Zn-0.1NMP holding minor advantages at some current settings. However, this minor advantage quickly disappeared as Zn-0.1NMP samples' performance quickly decayed and eventually failed in the long cycling test shown in Figure 2e. The Zn-0.3NMP samples produced slightly worse performance, especially during the higher rate scans and the 2 m $Zn(OTF)_2$ sample has the worst performance under all rates. To align the performance of the system with $A_2R9Mg$ in Zn-0.2NMP electrolyte, their performances are also compared with other reported biomass-derived carbon electrodes in AZICs applications as shown in Table S1, Supporting Information.

**Batteries & Supercaps**

Research Article
doi.org/10.1002/batt.202500161

**Chemistry Europe**
European Chemical
Societies Publishing

A long cycling test was also performed to evaluate the effect of different electrolytes over cycling life. As demonstrated in Figure 2e, when tested at $1 \text{ A g}^{-1}$, Zn-0.2NMP and Zn-0.3NMP could last 50 000 cycles, while all others failed before 10 000 cycles. Between Zn-0.2NMP and Zn-0.3NMP samples, the Zn-0.2NMP sample demonstrated a much better capacity retaining capability, 76.3% of the first cycle's capacity at the 50 000th cycle. In contrast, the Zn-0.3NMP sample could only retain 49.6% of its original capacity. It was also observed that the sample with modified Zn-0.2NMP electrolyte had superior stability even after long cycling and degradation (Figure 2e). The performance of the Zn-0.3NMP sample fluctuated at around 35 000 cycles and worsened as the cycling process continued. In addition, to align samples' cycling and charge storage performance with standard practice in the field, Figure 2d–f shows plotted in terms of Wh kg$^{-1}$ and supplied in Figure S5, Supporting Information, in which 2 m Zn(OTF)$_2$ Zn-0.1NMP, Zn-0.2NMP, and Zn-0.3NMP samples showed 44.55, 58.98, 65.98, and 50.70 Wh kg$^{-1}$, respectively.

To study the effect of NMP additive over the cell characteristics during different cycles, an EIS test was performed for samples using standard Zn(OTF)$_2$ electrolyte and Zn-0.2NMP electrolyte. As indicated in Figure S3, Supporting Information, both cells were tested at $1 \text{ A g}^{-1}$, and EIS data was sampled at 0, 600, and 900 cycles, respectively. As indicated in Figure S3, Supporting Information, the cell with Zn-0.2NMP electrolyte consistently showed higher resistance than the standard electrolyte and had drastically larger ionic conductivity at 0 cycles—an effect due to lowered ion-transfer kinetics induced by

the potentially enlarged solvating size of the ion complex. However, at 900 cycles, cells with the standard electrolyte have failed, and their ionic conductivity has dramatically decreased, likely due to uncontrolled overgrowing of the solid–electrolyte interface.[32] SEM was performed on both, the zinc electrode and the active carbon electrode as shown in Figure S6, Supporting Information. The surface of active carbon electrode did not indicate an apparent visual difference in terms of structure (Figure S6c,d, Supporting Information). However, distinct flower-like dendrites can be seen on the zinc electrode surface from the sample without addition of NMP (Figure S6a, Supporting Information). At the meantime, the surface of zinc electrode that was working with Zn-0.2NMP electrolyte remains compact and relatively smooth (Figure S6b, Supporting Information). Such difference in zinc electrode surface morphology suggests the unstable nature of zinc in aqueous electrolytes,[33] in this case, 2 m Zn(OTF)$_2$ electrolyte, and the improvement in stability after NMP is introduced. Considering the drastically improved long-term stability, electrode protection, and cycle life of 50 000 cycles at $1 \text{ A g}^{-1}$, the slight trade-off over ionic conductivity caused by NMP is within acceptable range.

To demonstrate the potential of using A$_2$R9Mg and Zn-0.2NMP electrolyte in scaled-up applications, a 2 cm × 2 cm pouch cell (≈1.83 mg cm$^{-2}$) was assembled and tested. When comparing the variable rate of CV performance between the coin cell and the pouch cell (**Figure 3**a,b), the pouch cell delivered a very similar performance profile to the coin cell at each rate, and current density for both cells was also nearly identical at different voltage rates.
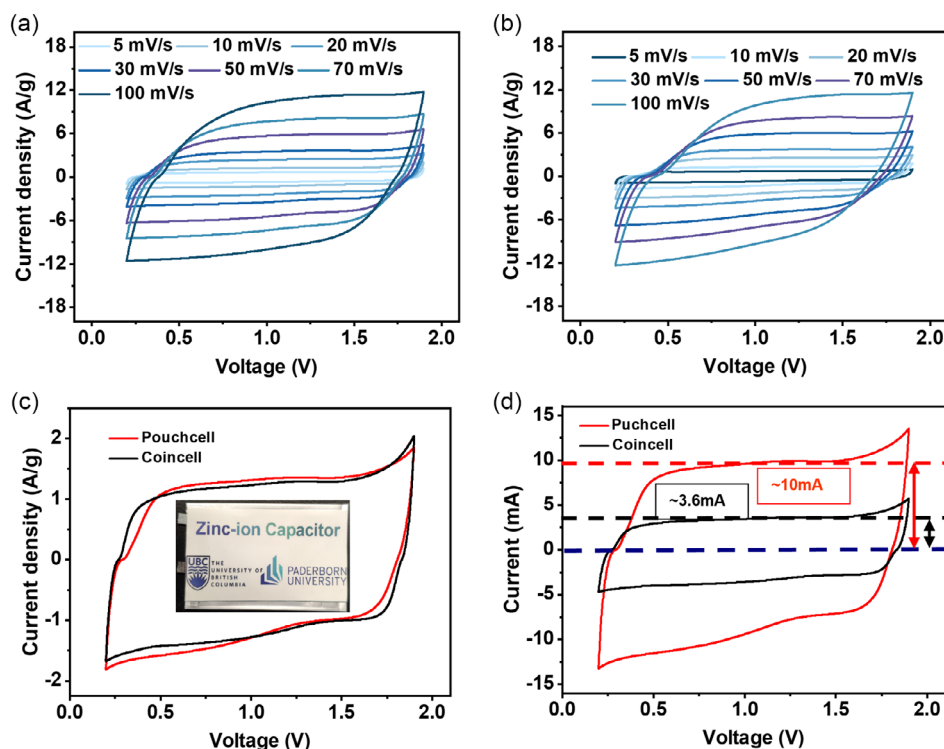


**Figure 3.** CV curves of A$_2$R9Mg with Zn-0.2NMP electrolyte in a) coin cells at rate scans of 5–100 mV s$^{-1}$, b) 2 cm × 2 cm pouch cell format, c) single cycle at 10 mV s$^{-1}$ from coil cell and pouch cell with a pouch cell picture, and d) single cycle at 10 mV s$^{-1}$ from coin cell and pouch cell without normalization.

**Batteries & Supercaps**

Research Article
doi.org/10.1002/batt.202500161

**Chemistry Europe**
European Chemical
Societies Publishing

To investigate the electrochemical kinetics in both the coin cell and pouch cell, the Buhn method was used to calculate diffusive and capacitive contributions, where the function used is as below

$$I = k_1 v + k_2 v^{0.5} \tag{1}$$

where $k_1$ and $k_2$ are constants and $k_1 v$ and $k_2 v^{0.5}$ are the current contributions of the capacitive and diffusion controlled processes, respectively. Using CV scan data at different rate, and $k_1$ and $k_2$ calculated in Figure S7, Supporting Information, each type of contributions is calculated and plotted in Figure S8, Supporting Information. The dominant charge storage mechanism is mainly capacitive at all scan rates, being at 67% of contributions under a low rate of $5\,mV\,s^{-1}$, and increased to 90% at $100\,mV\,s^{-1}$. Pouch cell shared an almost identical behavior as the coin cell, only 1% drop in capacitive contribution at $5\,mV\,s^{-1}$, suggesting that the change in packaging format and cell size did not alter the electrochemical kinetics of the system.

The scan rate at $10\,mV\,s^{-1}$ for both samples was isolated and displayed in Figure 3c. As expected, the pouch cell showed a much higher current response during the charge at around 10 mA, roughly 2.77 times the coin cell's current at $\approx3.6$ mA (Figure 3d). A cycling test was performed on the pouch cell at $1\,A\,g^{-1}$ and the result was compared with the coin cell cycling performance in Figure S9, Supporting Information. The pouch cell demonstrated a stable specific capacitance and energy density at $131.2\,F\,g^{-1}$ and $52.7\,Wh\,kg^{-1}$, respectively. This further proves the potential of large-scale applications of A$_2$R9Mg AC electrodes and Zn-0.2NMP electrolytes in pouch cell setups.

## 3. Conclusion

This study presents a sustainable precursor-derived carbon as a high-performance viable alternative to conventional ACs. Utilizing a eutectic template strategy, we successfully synthesized a mesopore-enriched AC material with a well-developed porous structure. The mesopores significantly enhanced ion transport and adsorption/desorption kinetics, contributing to the material's outstanding electrochemical performance. The assembled AZIC achieved a high specific capacity of $164.39\,F\,g^{-1}$ at $0.1\,A\,g^{-1}$ and exhibited exceptional cycling stability, retaining 94.5% of its capacitance over 50 000 cycles. Furthermore, a pouch-cell prototype was fabricated, delivering promising results that underscore the feasibility of large-scale practical applications. These findings emphasize the critical role of mesopore-rich carbon materials in advancing scalable and high-performance energy storage systems.

## 4. Experimental Section

### Material Fabrication

Adenine (purity >99 %) and D-(−)-ribose (analytical grade) were sourced from TCI EUROPE N.V. and Serva, respectively. MgCl$_2$·6H$_2$O ($\geq$99%) and calcium chloride dihydrate ($\geq$99%) were obtained from Carl Roth and Fisher Chemicals. All chemicals were used without further purification.

For the synthesis of AR$_2$9Ca, a typical procedure involved grinding adenine (1.28 g) and ribose (1.56 g) in a 1:2 molar ratio with CaCl$_2$·2H$_2$O (20 g). The resulting mixture was placed in a crucible and heat treated at 900 °C for 2 h with a heating rate of $1\,°C\,min^{-1}$ under a nitrogen atmosphere. Upon cooling to room temperature, the product was washed twice with HCl (1 M, $\approx$400 mL) at room temperature and once at 70 °C, followed by two washes with distilled water. The material was dried at 60 °C at atmospheric pressure for several hours, followed by vacuum drying at 150 °C overnight to remove absorbed moisture. The final product, yielding $\approx$22%, was labeled based on the adenine (A) to ribose (R) molar ratio, using a subscript number "2" following behind letter "A" or "R" accordingly, with the number "9" indicating the pyrolysis temperature (900 °C) and the final suffix representing the salt used (Mg as MgCl$_2$·6H$_2$O, Ca as CaCl$_2$·2H$_2$O). For example, AR$_2$9Mg represented the final product synthesized from adenine and ribose (1:2 molar ratio) at a pyrolysis temperature of 900°C with the MgCl$_2$·6H$_2$O salt.

### Material Structure Characterization

Materials were thoroughly washed with 1M hydrochloric acid to remove potential impurities and to neutralize them. TEM images were obtained from a FEI Talos F200X G2 system. SEM images were recorded on a LEO 1550-Gemini SEM from Zeiss. Nitrogen adsorption and desorption isotherms at 77 K were recorded on a Quadrasorb SI apparatus. The samples were degassed at 150 °C under vacuum for 20 h before the measurements. The BET method was used to calculate the specific surface area ($S_{BET}$) from nitrogen adsorption–desorption isotherm ($P/P_0 <0.2$). The $V_T$ was obtained from the amount of gas adsorbed at $P/P_0 = 0.995$. Pore size distribution and volumes of micropores and mesopores were calculated by the quenched solid density functional theory (QSDFT) model using slit/cylindrical pore shape.

### Electrochemical Performance

Electrodes were prepared by mixing active material with acetylene black (AB) and polytetrafluoroethylene binder at an 8:1:1 weight ratio, pressed into free-standing electrode sheets, and cast on the carbon fiber cloth. After drying, it was punched into 12 mm-diameter round pieces and assembled into CR3032 coin cells with zinc foil on the opposite side for testing. Electrochemical measurements such as CV, galvanic charge–discharge (GCD) tests, and EIS were performed using a Biologic VSP-3e potentiostat and cycling tests were performed on a NEWARE BTS 4000 battery cycler.

## Conflict of Interest

The authors declare no conflict of interest.

## Data Availability Statement

The data that support the findings of this study are available in the supplementary material of this article.

[1] X. Wang, F. Wan, L. Zhang, Z. Zhao, Z. Niu, J. Chen, *Adv. Funct. Mater.* **2018**, *28*, 1707247.

[2] J. Yang, H. Tian, Y. Li, H. Li, S. Li, H. Yang, M. Ding, X. Wang, P. Y. Chen, *Energy Storage Mater.* **2022**, *53*, 352.

[3] J. Chen, Q. Wang, S. Pan, Z. Lu, Y. Fu, *J. Energy Storage* **2024**, *104*, 114417.

[4] B. Wang, Y. Yue, F. Zuo, S. Wang, Z. Zhang, Y. Zhang, M. Liu, H. Zhang, *Chem. Catal.* **2024**, *4*, 101108.

[5] Y. Chen, Z. Song, Y. Lv, L. Gan, M. Liu, *Nano-Micro Lett.* **2025**, *17*, 117.

[6] H. Tang, J. Yao, Y. Zhu, *Adv. Energy Mater.* **2021**, *11*, 2003994.

[7] Z. Li, Y. An, S. Dong, C. Chen, L. Wu, Y. Sun, X. Zhang, *Energy Storage Mater.* **2020**, *31*, 252.

[8] D. Wang, L. Sheng, M. Jiang, X. Jin, X. Lin, S. Y. Lee, J. Shi, W. Chen, *Battery Energy* **2022**, *1*, 20220017.

[9] M. Li, Z. Li, X. Wang, J. Meng, X. Liu, B. Wu, C. Han, L. Mai, *Energy Environ. Sci.* **2021**, *14*, 3796.

[10] W. Yan, X. Cai, F. Tan, J. Liang, J. Zhao, C. Tan, *Chem. Commun.* **2023**, *59*, 1661.

[11] M. Winter, R. J. Brodd, *Chem. Rev.* **2004**, *104*, 4245.

[12] G. Sun, H. Yang, G. Zhang, J. Gao, X. Jin, Y. Zhao, L. Jiang, L. Qu, *Energy Environ. Sci.* **2018**, *11*, 3367.

[13] K. Xie, K. Ren, Q. Wang, Y. Lin, F. Ma, C. Sun, Y. Li, X. Zhao, C. Lai, *eScience* **2023**, *3*, 100153.

[14] X. Lu, L. Tao, K. Qu, Y. Zhang, C. Liu, R. Godin, J. Liu, *J. Mater. Chem. A* **2022**, *10*, 20273.

[15] J. Pampel, A. Mehmood, M. Antonietti, T. P. Fellinger, *Mater. Horiz.* **2017**, *4*, 493.

[16] C. Li, E. Lepre, M. Bi, M. Antonietti, J. Zhu, Y. Fu, N. López-Salas, *Adv. Sci.* **2023**, *10*, 2300526.

[17] C. Li, Z. Song, M. Liu, E. Lepre, M. Antonietti, J. Zhu, J. Liu, Y. Fu, N. López-Salas, *Energy Environ. Sci.* **2024**, *7*, e12695.

[18] W. Fan, J. Ding, J. Ding, Y. Zheng, W. Song, J. Lin, C. Xiao, C. Zhong, H. Wang, W. Hu, *Nano-Micro Lett.* **2021**, *13*, 1.

[19] P. Yu, Y. Zeng, Y. Zeng, H. Dong, H. Hu, Y. Liu, M. Zheng, Y. Xiao, X. Lu, Y. Liang, *Electrochim. Acta* **2019**, *327*, 134999.

[20] W. Yu, H. Wang, S. Liu, N. Mao, X. Liu, J. Shi, W. Liu, S. Chen, X. Wang, *J. Mater. Chem. A* **2016**, *4*, 5973.

[21] J. Yin, W. Zhang, N. A. Alhebshi, N. Salah, H. N. Alshareef, *Adv. Energy Mater.* **2021**, *11*, 2100201.

[22] D. Wang, Z. Pan, G. Chen, Z. Lu, *Electrochim. Acta* **2021**, *379*, 138170.

[23] D. Xue, D. Zhu, H. Duan, Z. Wang, Y. Lv, W. Xiong, L. Li, M. Liu, L. Gan, *Chem. Commun.* **2019**, *55*, 11219.

[24] L. Qie, Y. Lin, J. W. Connell, J. Xu, L. Dai, *Angew. Chem. Int. Ed.* **2017**, *56*, 6970.

[25] N. Shimodaira, A. Masui, *J. Appl. Phys.* **2002**, *92*, 902.

[26] Y. Xu, C. Zhang, M. Zhou, Q. Fu, C. Zhao, M. Wu, Y. Lei, *Nat. Commun.* **2018**, *9*, 1720.

[27] H. Jia, J. Sun, X. Xie, K. Yin, L. Sun, *Carbon* **2019**, *143*, 309.

[28] L. Dong, X. Ma, Y. Li, L. Zhao, W. Liu, J. Cheng, C. Xu, B. Li, Q. H. Yang, F. Kang, *Energy Storage Mater.* **2018**, *13*, 96.

[29] Z. Tian, F. Lai, T. Heil, S. Cao, M. Antonietti, *Sci. China Mater.* **2020**, *63*, 748.

[30] D. Wang, G. Fang, T. Xue, J. Ma, G. Geng, *J. Power Sources* **2016**, *307*, 401.

[31] X. Yang, C. Hu, Y. Chen, Z. Song, L. Miao, Y. Lv, H. Duan, M. Liu, L. Gan, *J. Energy Storage* **2024**, *104*, 114509.

[32] X. Geng, X. Hou, X. He, H. J. Fan, *Adv. Energy Mater.* **2024**, *14*, 2304094.

[33] D. Zhang, L. Miao, Z. Song, X. Zheng, Y. Lv, L. Gan, M. Liu, *Energy Fuels* **2024**, *38*, 12510.